Journal Pre-proof

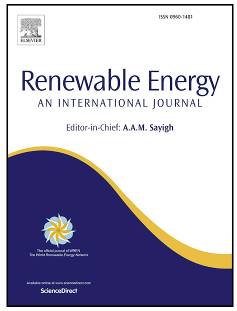

Numerically efficient fatigue life prediction of offshore wind turbines using aerodynamic decoupling

Chao Chen, Philippe Duffour, Paul Fromme, Xugang Hua

PII: S0960-1481(21)00981-2

DOI: https://doi.org/10.1016/j.renene.2021.06.115

Reference: RENE 15640

To appear in: *Renewable Energy*

Received Date: 13 January 2021

Revised Date: 7 June 2021

Accepted Date: 8 June 2021

Chao Chen: Conceptualization, Methodology, Formal analysis, Software, Validation, Writing - Original Draft

Philippe Duffour: Conceptualization, Methodology, Writing - Review & Editing

Paul Fromme: Conceptualization, Methodology, Writing - Review & Editing

Xugang Hua: Methodology, Writing - Review & Editing, Funding acquisition

Numerically efficient fatigue life prediction of offshore wind turbines using aerodynamic decoupling

Chao Chen[1], Philippe Duffour[2], Paul Fromme[3], and Xugang Hua[1*]

[1]Key Laboratory for Wind and Bridge Engineering, Hunan University, Changsha, China
[2]Department of Civil, Environmental and Geomatic Engineering, University College London, United Kingdom
[3]Department of Mechanical Engineering, University College London, United Kingdom

[*]Corresponding author: cexghua@hnu.edu.cn

Numerically efficient fatigue life prediction of offshore wind turbines using aerodynamic decoupling

Abstract

The fatigue life prediction for offshore wind turbine support structures is computationally demanding, requiring the consideration of a large number of combinations of environmental conditions and load cases. In this study, a computationally efficient methodology combining aerodynamic decoupling and modal reduction techniques is developed for fatigue life prediction. Aerodynamic decoupling is implemented to separate the support structure and rotor-nacelle assembly. The rotor dynamics were modelled using an aerodynamic damping matrix that accurately captures the aerodynamic damping coupling between the fore-aft and side-side motions. Soil-structure interaction is modelled using p-y curves, and wave loading calculated based on linear irregular waves and Morison's equation at a European (North Sea) site. A modal reduction technique is applied to significantly reduce the required number of degrees of freedom, allowing the efficient and accurate calculation of hotspot stresses and fatigue damage accumulation. The modal model was verified against a fully coupled model for a case-study, monopile supported offshore wind turbine in terms of response prediction and fatigue life evaluation. The modal model accurately predicts fatigue life (within 2%) for a range of parameters at a fraction of computational cost (0.5%) compared to the fully coupled model.

Key words: offshore wind turbines; fatigue life prediction; aerodynamic damping; modal analysis.

1 Introduction

As the size of Offshore Wind Turbines (OWTs) has been increasing in order to generate electricity more efficiently, they have become more susceptible to large amplitude vibration and fatigue damage [1]. Therefore, an accurate prediction of fatigue life at the preliminary design stage is required. At present, there are many wind turbine modelling software packages available, and most of them employ fully coupled models in which different components of OWTs are coupled based on multibody dynamics. In the literature, many researchers used these fully coupled models to conduct fatigue damage calculation for OWTs [2]. For example, Koukoura et al. [3] studied the influence of wind-wave misalignment on fatigue in the OWT support structure. Their simulations were performed using HAWC2 [4], which is an aeroelastic software based on multibody formulation. Velarde et al. ([5][6]) also used HAWC2 to study the fatigue sensitivity and reliability of OWTs supported by gravity foundations and monopiles. Marino et al. [7] focused on the influence of alternative wave models when calculating wind turbine fatigue loads. The aero-servo-elastic software FAST [8] developed by NREL combined with an external hydrodynamic module was used by Hübler et al. [9] to obtain dynamic responses. They developed fatigue assessment methodologies for OWTs considering scattering environmental conditions. FAST modified to include Soil-Structure Interaction (SSI) matrices was used to conduct time domain simulations. Horn et al. [10] introduced a stochastic model to assess the fatigue reliability of an OWT. They used a fully coupled finite-element code USFOS/VpOne to establish the numerical model of a bottom-fixed monopile-mounted OWT.

A large number of environmental states and load cases needs to be considered when calculating the fatigue life of OWT support structures [11], requiring a significant computational effort. In a comprehensive fatigue analysis, the OWT structural response needs to be computed and analysed for each of the combinations of environmental parameters, leading to thousands of simulations [12]. In order to accelerate the fatigue prediction, many studies concentrated on the reduction of the number of load cases ([11][13][14][15]) or developing novel methods ([12][16]) to reduce the simulation requirements. Stieng and Muskulus [15] proposed a method of reducing the number of required environmental states, based on importance sampling and a specially adapted two-stage filtering procedure, from which pseudo-optimal sets of load cases can be used to conduct the fatigue assessment of the monopile. Wilkie and Galasso [16] developed a computational framework to conduct the OWT fatigue reliability analysis, using Gaussian process regression to develop surrogate models of load-induced fatigue damage, which allows the reduction of the computational effort with high accuracy. Conducting the fatigue analysis of OWTs in the frequency domain

[17] significantly reduces the computational effort but is generally not as accurate as the time domain analysis. On the other hand, fully coupled models are usually more computationally intensive as the interaction between many components along with the environmental loading needs to be considered. In some cases, detailed Finite Element (FE) models of the support structures are required, but it is often not possible to implement those in current wind turbine modelling packages. As a result, a simplified decoupling approach is desirable for faster fatigue analysis. A common model simplification is to lump the mass of the Rotor-Nacelle Assembly (RNA) at the top of the flexible tower and apply the aerodynamic resultant thrust together with a dashpot or an equivalent Rayleigh damping model to represent the aerodynamic damping [18]. For instance, Dong et al. ([19][20]) imported aerodynamic loading from HAWC2 to USFOS to obtain the dynamic response of a jacket support structure in a 5 MW OWT and analysed the long-term fatigue accumulation. Rezaei et al. ([21][22]) studied the sensitivity of fatigue life of OWTs to damping and scour. They developed a detailed FE model in Abaqus including nonlinear soil springs, and aerodynamic loads calculated by FAST. Muskulus [23] and Schafhirt and Muskulus [24] decoupled the wind turbine system by separating the aerodynamic thrust into a static mean force, a dynamic turbulent force and a dynamic damping force. A simple expression for the thrust was obtained by fitting a thrust coefficient to fully coupled simulation results.

The definition of the aerodynamic damping in decoupled wind turbine models is usually based on damping ratios. The determination of damping ratios can be based on theoretical predictions ([25][26][27]) or measurements ([28][29][30][31][32]). However, using damping ratios separately in the Fore-Aft (FA) and Side-Side (SS) directions to represent the aerodynamic damping in OWTs implicitly ignores the influence of damping coupling between the two directions. Tarp-Johansen et al. [33] found that the aerodynamic damping for the first lateral tower mode (in the SS direction) is different for a normal tower configuration (the tower FA and SS motions both allowed) and a stiff downwind tower configuration (the tower FA motion not allowed). Studies by Chen et al. ([34][35]) emphasised the importance of the coupling between the FA and SS motions and developed a decoupled wind turbine model with an aerodynamic damping matrix to capture this coupling.

In summary, most studies in literature concentrated on reducing the number of load cases or developing more advanced statistical models to accelerate the fatigue analysis of OWTs. Among the relatively few studies using simplified decoupling models to conduct fatigue analyses, the inclusion of aerodynamic damping was usually implemented by using aerodynamic damping ratios, not considering the important aerodynamic damping coupling between the FA and SS motions. There is a need for computationally efficient ways of calculating fatigue life of OWTs with more advanced decoupled models. This paper proposes a novel methodology, extending a previously developed model based on modal reduction and aerodynamic damping decoupling to include all relevant features such as soil-structure interaction and key dynamic couplings. It is organised as follows. Section 2 presents the reference monopile supported OWT which is used as a case study. The fully coupled model developed in Matlab used for reference predictions is described. Section 3 introduces the development of the decoupled full model with rigid blades and describes the modal reduction from the fully coupled model. Section 4 details the calculation of the stress time history given dynamic responses and the fatigue estimation method. Section 5 provides the fatigue life results and explores the effect of varying structural damping. Section 6 concludes the paper.

2 Fully coupled reference model

In the present study, a fully coupled aeroelastic model of a case study monopile-supported OWT was implemented in Matlab and used as a reference model against which reduced models are later compared. This structural model is a FE formulation including the blades, tower and monopile (Section 2.1) with soil springs as described in Section 2.2 representing SSI. The aerodynamic forces, presented in Section 2.3, were computed using unsteady Blade Element Momentum (BEM) theory. The hydrodynamic force calculation is based on Morrison's equation, described in Section 2.4. The OWT model is based on the widely used 5MW reference monopile-supported offshore wind turbine published by NREL [36]. The basic properties of this OWT are listed in Table 1 and a schematic of it is shown in Fig. 1. The combination of the tower, transition piece, and monopile foundation is defined as the support structure of the OWT, which supports the RNA. The motivations for developing a bespoke model were the ability to include SSI, as this is an important feature in monopile-supported OWTs, and taking advantage of the improved accuracy of the FE formulation.

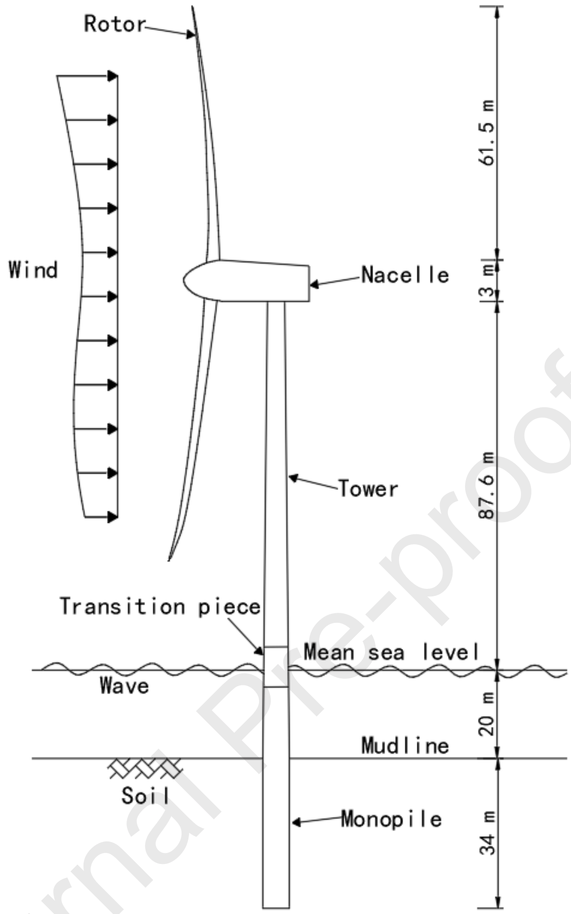

Fig. 1. Schematic of the NREL 5MW reference OWT.

2.1 ***Finite Element Model***

In the FE model, the tower, blades and monopile were modelled using three-dimensional Euler-Bernoulli beam elements. The numbers of beam elements for the single blade, tower and monopile are 17, 11 and 26 respectively, bringing the total number of beam elements is 88. For each node, there are six DOFs corresponding to three translational motions and three rotational motions. A convergence study confirmed that the beam element number is sufficient. Given the material and geometrical properties of the beam elements, the equations of motion of the OWT model can be formulated by:

$$\begin{aligned}\mathbf{M}(t)\ddot{\mathbf{u}}(t) + (\mathbf{C}_{Struc}(t) + \mathbf{C}_{Soil}(t))\dot{\mathbf{u}}(t) + \mathbf{K}(t)\mathbf{u}(t) \\ = \mathbf{F}_{Wind}(t) + \mathbf{F}_{Wave}(t),\end{aligned} \tag{1}$$

where $\mathbf{M}(t), \mathbf{K}(t)$ are the mass and stiffness matrices, $\mathbf{C}_{Struc}(t)$ and $\mathbf{C}_{Soil}(t)$ are the viscous damping matrices representing structural damping and soil damping respectively, $\mathbf{u}(\mathrm{t})$ is the displacement vector, $\mathbf{F}_{Wind}(t)$ and $\mathbf{F}_{Wave}(t)$ are the wind force and wave force vectors. $\mathbf{M}(t)$ and $\mathbf{K}(t)$ are time dependent matrices [37] when the OWT is operating, as the rotation of the blades was taken into consideration by introducing a time dependent transformation when assembling the global matrix from the local elemental matrices. The structural damping and soil damping in this study are both assumed to be proportional Rayleigh damping using the relationship $\mathbf{C} = \alpha\mathbf{M} + \beta\mathbf{K}$, where α and β are Rayleigh coefficients. These were determined such that the total damping ratios due to the structural damping in the support structure and the soil damping were 1.5% according to [38]. The structural damping of a single blade was selected as 0.48%, following the default FAST setting. Note that the structural and soil damping matrices are time dependent, as they are proportional to the time-dependent mass and stiff matrices. The contribution of hydrodynamic damping and the aerodynamic damping of the tower are small compared to other damping sources [38] and therefore were not included [33].

The nacelle was modelled using a lumped mass at the tower top, added to the mass matrix. For simplicity, the gravitational centre of the nacelle was located at the tower top, so that moments of inertia of the nacelle about all axes are zero. Time domain analyses were conducted by implementing the numerical integration scheme HHT-α [39], which is a generalised version of the Newmark-β method.

Table 1 Basic properties of the NREL 5MW reference OWT, based on [36].

Rotor Diameter, R	126 m
Hub Radius, r_{hub}	1.5 m
Hub Height from Mean Sea Level (MSL)	87.6 m
Water Depth (MSL?), h	20 m
Monopile Embedded Length	34 m
Tower Diameter, D_{Tower}	3.87-6.00 m
Tower Thickness, t_{Tower}	19-60 mm
Monopile Diameter, D_{Pile}	6 m
Monopile Thickness, t_{Pile}	60 mm
Lumped Mass at Top	350×10^{3} kg

Natural Frequency for the First Bending Mode of the Support Structure	0.24-0.25 Hz
Natural Frequency for the Second Mode of the Support Structure	1.74-1.75 Hz

2.2 ***Soil model***

The soil profile used in this study is a layered combination of sandy soils typical for a European offshore site for which the 5MW OWT model was developed. The soil profile combines loose sand, medium sand, and dense sand from bottom to the pile head with thicknesses of 14m, 14m, and 6m respectively, based on the data provided in Appendix B in [40]. The soil properties are listed in Table 2.

Table 2 Mechanical properties of the soil profiles used in the model.

Soil type	Density γ (1×10^3 kg/m^3)	Poisson's ratio ν	Friction angle φ	Shear modulus G_s (MPa)	Shear wave velocity V_s (m/s)	Elastic modulus E_s (MPa)
Loose sand	1.75	0.30	33º	47	164	18
Medium sand	1.90	0.30	36º	109	240	42
Dense sand	2.07	0.30	38º	182	297	70

The SSI was modelled using p-y curves recommended in DNVGL-RP-C212 [41], where p is the resistance (pressure) from the surrounding soil when the pile deflects laterally by distance y. The p-y relationship for a vertical pile in cohesionless soil can be established using the following equation:

$$p = Ap_u \tanh\left(\frac{k_m Z}{Ap_u} y\right), \tag{2}$$

where k_m is the initial modulus of subgrade reaction, A is a factor to account for static or cyclic loading conditions, Z is the depth below the surface. This study adopted the cyclic loading condition, as fatigue calculation corresponds to the cyclic vibration of the monopile. The ultimate static lateral resistance, p_u, is defined as:

$$p_u = \min\begin{cases} (C_1 Z + C_2 D_{Pile})\gamma' Z, \\ C_3 D_{Pile}\gamma' Z, \end{cases} \tag{3}$$

where, C_1, C_2 and C_3 depend on the friction angle of the soil, D_{Pile} is the diameter of the monopile.

In the model, the soil was modelled by a series of horizonal soil springs characterised by Eq. (2) at different heights of the monopile foundation. The soil springs were located at the nodes of the monopile. The displacements of the nodes of the monopile were calculated given the average forces in the FA and SS directions. Then the soil springs were introduced by directly inserting the spring stiffness coefficients into the system stiffness matrix at relevant locates. In order to be consistent with the modal analysis, which will be introduced in Section 3.2, the soil springs were set to be linear such that the soil stiffness coefficients were kept constant during the time integration.

2.3 *Wind loading*

The wind loading calculation is based on classic unsteady Blade Element Momentum (BEM) theory ([42][43]) with corrections. The iteration loop in a steady BEM code is neglected in the unsteady BEM code since the iteration is replaced by a time evolution, assuming that the time step chosen is sufficiently small. The corrections adopted in the unsteady BEM code include Prandtl and Glauert corrections [42]. To be consistent with the derivation leading to the aerodynamic damping matrix (described in Section 3), other corrections such as skew wake and dynamic wake corrections are not included in the unsteady BEM code.

A non-uniform turbulent inflow wind field was used as the input to the unsteady BEM code to calculate the aerodynamic forces acting on the blade elements. A customised turbulent wind field generator was coded in Matlab, producing similar wind time series compared to the wind field generator in FAST, TurbSim [44]. The Kaimal spectrum was used to generate the turbulent wind field, and its relevant parameters (e.g., coherence length parameters) were selected as recommended by IEC 61400-3 [45]. The relationship between turbulence intensities and mean wind speeds at hub height was defined according to the Normal Turbulence Model (NTM). Medium turbulence intensity (Category B) was assumed.

The inflow wind velocities, the velocity caused by rotor rotation and the velocities caused by blade vibration were used as input to the unsteady BEM code. The unsteady code calculated the instantaneous local aerodynamic forces for all blade elements at every time step in the time integration. The aerodynamic force calculation based on the customised wind field generator and the unsteady BEM code was successfully verified against FAST (results not shown).

2.4 *Wave loading*

Morison's equation was used for the wave loading calculation. The wave force applied to the monopile is a combination of a viscous drag force and an inertia force which can be expressed by

$$F_{wave} = \frac{1}{2}\rho_w D_{Pile} C_d |\dot{u}_w| \dot{u}_w + \frac{\pi}{4}\rho_w D_{Pile}^2 C_m \ddot{u}_w, \tag{4}$$

where $\dot{u}_w$ and $\ddot{u}_w$ are the velocity and acceleration of water particles, C_d is the drag coefficient, D_{Pile} is the diameter of the monopile between the mean sea level and the mudline, C_m is the inertia coefficient and ρ_w is the density of water. C_d and C_m were chosen as 1 and 2 respectively as the recommended values in [46]. The velocities caused by monopile vibration were ignored in the wave loading calculation as the monopile vibration velocities are much smaller than the wave particle velocities.

The wave profile is irregular and obtained by the superposition of wave components following linear wave theory and JONSWAP spectrum [47]. For a particular frequency point f, the JONSWAP spectrum definition is given by

$$S_{JS} = S_{PM}(f) \cdot (1 - 0.287\ln(\gamma)) \cdot \gamma^{\exp\left[-\frac{(f-f_p)^2}{2\sigma^2 f_p^2}\right]}, \tag{5}$$

where

$$S_{PM}(f) = 0.3125 H_s^2 T_p \left(\frac{f}{f_p}\right)^{-5} \exp\left[-1.25\left(\frac{f}{f_p}\right)^{-4}\right]. \tag{6}$$

f_p is the peak frequency defined as $1/T_p$, H_s is the significant wave height, γ is the peak-shape parameter, which is assumed to be equal to 3.3 for the North Sea conditions according to [47], σ is the spectral width parameter. T_p is the wave peak period. The wave elevation, velocity and acceleration time series can be obtained by summing wave components corresponding to different wave frequencies. Combining Morison's equation and the linear irregular waves defined above, the wave forces were defined in the external wave force vector in Eq. (1).

3 Reduction to modal OWT model

3.1 *Decoupled model*

The fully coupled model described in Section 2 can be decoupled by computing the resultants of the aerodynamic wind-rotor interaction at the tower top. This decoupling is briefly summarised here. It was described in more detail in [35] and [48] for onshore wind turbines, where wave loading and SSI were not considered. The decoupling process starts with the linearisation of the resultant aerodynamic forces from the rotor into static forces and damping forces proportional to the tower top velocities, assuming rigid blades. These linearised aerodynamic forces are then applied on the RNA mass lumped at the tower top and the dynamic responses of the finite element model of the OWT support structure can be obtained, excluding the analysis of blade vibration. This is schematically illustrated in Fig. 2. An aerodynamic damping matrix is introduced when calculating the damping forces. This decoupling process results in a decoupled model with rigid blades and simplifies the calculation of aerodynamic forces applied to the rotor.

When the OWT is in operation, the tower, transition piece and monopile foundation mainly vibrate in the FA direction (x) and SS direction (y). Here the vertical vibration is neglected due to its insignificance in the decoupling process and its very small amplitude. The linear motions at the tower top are represented by $\dot{x}$ and $\dot{y}$, and the angular motions represented by $\dot{\theta}_x$ and $\dot{\theta}_y$ around the x and y axes respectively, which are defined in Fig. 2. The blades are assumed to be rigid and the blade vibration is ignored, so parametric excitations due to rotor dynamics are not included. Combining the BEM theory and tower dynamics, the aerodynamic forces applied to a flexible tower can be linearised to the sum of terms corresponding to the forces for an assumed rigid tower, plus terms proportional to the tower top linear and angular velocities, which can be expressed as

$$\mathbf{F}_{Top}^{Flex}(t) = \mathbf{F}_{Top}^{Rigid}(t) - \mathbf{C}_{Aero}\dot{\mathbf{u}}_{Top}(t). \quad (7)$$

The aerodynamic force resultants $\mathbf{F}_{Top}^{Flex}(t)$ are calculated at the tower top as forces and moments, as shown in Fig. 2. $\mathbf{F}_{Top}^{Rigid}(t)$ does not depend on the tower vibration. $\mathbf{C}_{Aero}$ is called the aerodynamic damping matrix, which captures the aerodynamic damping caused by the wind-rotor interaction considering the coupling between the tower top FA and SS motions. According to [48], $\mathbf{C}_{Aero}$ is

$$\mathbf{C}_{Aero} = \begin{bmatrix} c_{xx} & c_{xy} & c_{x\theta_x} & c_{x\theta_y} \\ c_{yx} & c_{yy} & c_{y\theta_x} & c_{y\theta_y} \\ c_{\theta_x x} & c_{\theta_x y} & c_{\theta_x\theta_x} & c_{\theta_x\theta_y} \\ c_{\theta_y x} & c_{\theta_y y} & c_{\theta_y\theta_x} & c_{\theta_y\theta_y} \end{bmatrix}, \tag{8}$$

where the off-diagonal terms representing the damping coupling between the FA and SS directions are not symmetric. The expression of $\mathbf{F}_{Top}^{Flex}(t)$ is detailed in Appendix A.

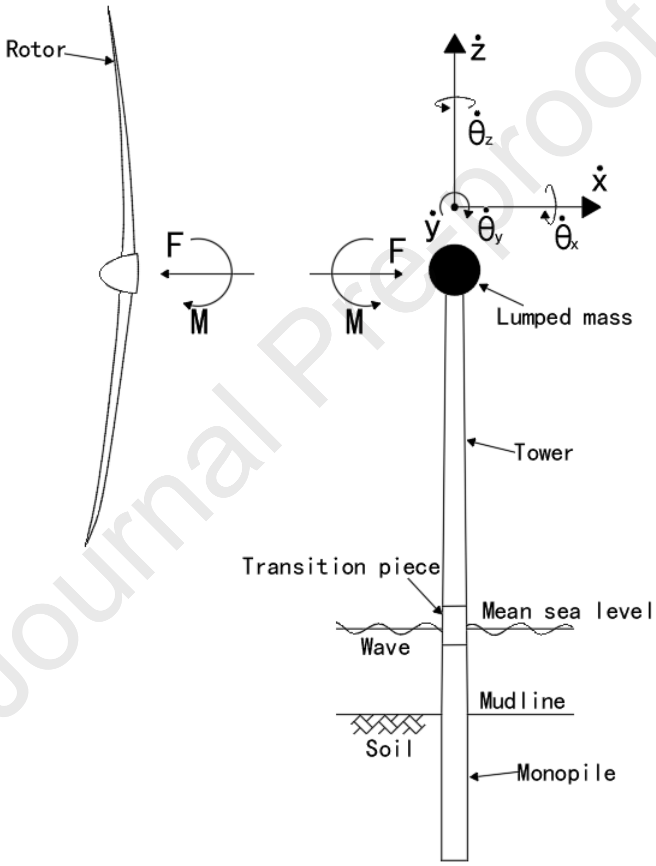

Fig. 2. Schematic illustrating the decoupling of the aerodynamic forces at tower top.

If the inflow wind field is turbulent and non-uniform, $\mathbf{C}_{Aero}$ is a time-varying matrix. To obtain a constant $\mathbf{C}_{Aero}$ and thus simplify the aerodynamic decoupling, $\mathbf{C}_{Aero}$ was calculated using an inflow wind field assumed to be uniform and constant at the mean wind speed. It has been shown in a previous study [48] that the overall dynamic responses from the model with the constant aerodynamic damping matrix agree well with those from the model with the time-varying aerodynamic damping matrix. For a particular set of mean wind speed, rotor rotation speed, and blade pitch angles, the aerodynamic damping matrix can be calculated by following the derivations in [35] and [48]. $\mathbf{F}_{Top}^{Rigid}(t)$ was calculated based on the non-uniform wind field and the unsteady BEM code.

The decoupled model with rigid blades is formed as follows. The blade masses are lumped together with the nacelle mass at the tower top, so the total number of beam elements reduces to 37 due to the exclusion of the blade elements. The static component of the condensed aerodynamic forces, $\mathbf{F}_{Top}^{Rigid}(t)$, can be directly applied at the tower top as an external force independent of the tower top velocities. As a result, the equations of motion for the decoupled model with rigid blades can be written as

$$\begin{aligned} \mathbf{M}'\ddot{\mathbf{u}}'(t) + (\mathbf{C}'_{Struc} + \mathbf{C}'_{Soil} + \mathbf{C}'_{Aero})\dot{\mathbf{u}}'(t) + \mathbf{K}'\mathbf{u}'(t) \\ = \mathbf{F}'^{Rigid}_{Wind}(t) + \mathbf{F}'_{Wave}(t), \end{aligned} \tag{9}$$

where $\mathbf{M}'$, $\mathbf{C}'_{Struc}$, $\mathbf{C}'_{Soil}$, $\mathbf{C}'_{Aero}$ and $\mathbf{K}'$ are the reduced mass, structural damping, soil damping, aerodynamic damping and stiffness matrices respectively. $\mathbf{C}'_{Aero}$ contains the terms in $\mathbf{C}_{Aero}$ in Eq. (8) at appropriate locations. $\mathbf{F}'^{Rigid}_{Wind}(t)$ is the external aerodynamic force vector which includes $\mathbf{F}_{Top}^{Flex}(t)$ at the nodes at the tower top. $\mathbf{u}'(t)$ is the reduced displacement vector, where the prime sign represents the reduced size of the matrices and vectors compared to those for the fully coupled model. The model described by Eq. (9) effectively reduces the fully coupled OWT system by using finite elements to only model the support structure and capturing the wind-rotor-tower interaction through the lumped mass at the top and the aerodynamic damping matrix.

3.2 *Modal model*

A partial decoupling can be obtained from the equations of motion in Eq. (9) using the normal (undamped) mode shapes. The undamped mode shape matrix $\mathbf{\Psi}$ can be computed from the eigen analysis of the mass and stiffness matrices $\mathbf{M}'$ and $\mathbf{K}'$. As the damping matrix is not used to compute $\mathbf{\Psi}$, the modes considered here are real. The reduced displacement vector $\mathbf{u}'(t)$ can then be written as the generalised coordinate vector $\boldsymbol{\alpha}(t)$ multiplied by the normal (undamped) mode shape matrix: $\mathbf{u}'(t) =$

$\boldsymbol{\Psi\alpha}(t)$. Multiplying the transpose of the modal shape matrix, $\boldsymbol{\Psi}^{\mathrm{T}}$, at both sides of Eq. (9), we obtain

$$\begin{aligned}\boldsymbol{\Psi}^{\mathrm{T}}\mathbf{M}'\boldsymbol{\Psi}\ddot{\boldsymbol{\alpha}}(t) + \boldsymbol{\Psi}^{\mathrm{T}}(\mathbf{C}'_{Struc} + \mathbf{C}'_{Soil} + \mathbf{C}'_{Aero})\boldsymbol{\Psi}\dot{\boldsymbol{\alpha}}(t) \\ + \boldsymbol{\Psi}^{\mathrm{T}}\mathbf{K}'\boldsymbol{\Psi\alpha}(t) \\ = \boldsymbol{\Psi}^{\mathrm{T}}\mathbf{F}'^{Rigid}_{Wind}(t) + \boldsymbol{\Psi}^{\mathrm{T}}\mathbf{F}'_{Wave}(t).\end{aligned} \tag{10}$$

The equation above can be written in concise form:

$$\begin{aligned}\bar{\mathbf{M}}\ddot{\boldsymbol{\alpha}}(t) + (\bar{\mathbf{C}}_{Struc} + \bar{\mathbf{C}}_{Soil} + \bar{\mathbf{C}}_{Aero})\dot{\boldsymbol{\alpha}}(t) + \bar{\mathbf{K}}\boldsymbol{\alpha}(t) \\ = \bar{\mathbf{F}}^{Rigid}_{Wind} + \bar{\mathbf{F}}_{Wave},\end{aligned} \tag{11}$$

where $\bar{\mathbf{M}}$ and $\bar{\mathbf{K}}$ are the modal mass and stiffness matrices, $\bar{\mathbf{C}}_{Struc}$, $\bar{\mathbf{C}}_{Soil}$ and $\bar{\mathbf{C}}_{Aero}$ are the modal structural, soil and aerodynamic damping matrices, $\bar{\mathbf{F}}^{Rigid}_{Wind}$ and $\bar{\mathbf{F}}_{Wave}$ are the modal wind force and wave force vectors. $\bar{\mathbf{M}}$ and $\bar{\mathbf{K}}$ are diagonal matrices due to orthogonality of the normal modes. As the structural damping and soil damping are considered as Rayleigh damping, $\bar{\mathbf{C}}_{Struc}$ and $\bar{\mathbf{C}}_{Soil}$ are also diagonal. However, as $\mathbf{C}'_{Aero}$ is not of a Rayleigh damping type, $\bar{\mathbf{C}}_{Aero}$ is neither symmetric nor diagonal. Therefore, $\bar{\mathbf{C}}_{Aero}$ causes coupling between different modes and different vibration directions. It is possible to consider a particular number of modes by truncating the matrices and vectors in Eq. (11). For example, if considering the first two bending modes of the support structure, the system matrix size becomes 4×4 and the decoupled model is reduced to a 4-DOF model. Theoretically, considering more modes results in more accurate dynamic responses. However, it was found that the dynamic responses of the OWT are dominated by the first two bending modes of the support structure. For simplicity, only the results from the 4-DOF model are shown and used later. The time history of the generalised modal coordinate $\boldsymbol{\alpha}(t)$ was obtained by solving Eq. (11) using the HHT-α time integration method. The dynamic responses of the whole tower and monopile were calculated using modal expansion described by $\mathbf{u}'(t) = \boldsymbol{\Psi\alpha}(t)$. If displacement-dependent p-y curves are implemented to calculate the soil reactions at every time step, a time-dependent stiffness matrix including soil stiffnesses is inevitably introduced, making the modal reduction infeasible. Therefore, the inclusion of the soil springs in the modal model was realised using constant soil spring stiffness corresponding to the slope of the p-y curve at the average monopile lateral displacement.

4 Fatigue damage prediction

For a given mean wind speed, the dynamic responses of the whole support structure can be obtained from the modal model just described after time integration. Then, for a specific hotspot, the stress time history is calculated from the dynamic as described in the following sections.

4.1 ***Stress calculation***

In the fully coupled model, the dynamic component of the normal stresses σ_{zz} at position (x, y) within a tower cross-section and at position z along the tower can be directly obtained from the internal forces and the cross-section properties. The axial stresses are made of a static component cause by the weight and a dynamic part caused by the dynamic part of the FA and SS bending moments. In the reduced modal model developed in Section 3.2, the displacement, velocity, and acceleration responses along the wind turbine support structure can be directly obtained by superposition, but further computation is necessary to obtain section stresses. Therefore, a method is needed to estimate the stress time history at arbitrary locations using the displacement, velocity and acceleration responses. Pelayo et al. [50] presented a method to extract the dynamic stress from the responses under dynamic loading and the modal parameters of a structure. This method was formulated for beams under uniaxial bending [50], but the stresses in the FA and SS directions need to be considered simultaneously for OWTs. Therefore, this method was extended here to enable the calculation of stresses for bending in two directions.

Using the finite element method, the displacements $u_x(z,t)$ and $u_y(z,t)$ in FA and SS directions at any arbitrary height z along an individual beam element can be approximated by

$$u_x(z,t) = \mathbf{N}^e(z)\mathbf{u}_x^e(t), \tag{12}$$

$$u_y(z,t) = \mathbf{N}^e(z)\mathbf{u}_y^e(t), \tag{13}$$

where $\mathbf{N}^e(z)$ is the elemental shape function vector, $\mathbf{u}_x^e(t)$ and $\mathbf{u}_y^e(t)$ are the nodal displacement vectors in x and y directions for the beam element. For a given cross-section-section and time, the Euler-Bernoulli bending strains are the product of the local curvatures and the distance from the neutral axis in each direction. The curvatures can be obtained from Eqs. (12) and (13) by differentiating the shape functions twice with respect to z. The resultant longitudinal stress at time t, position (x, y) within the cross-section and z along the tower, is then the linear superposition of the two strains multiplied by Young's Modulus E:

$$\sigma_{zz}(x,y,z,t) = -E\left(\mathbf{N}^{e''}(z)\mathbf{u}_x^e(t)x + \mathbf{N}^{e''}(z)\mathbf{u}_y^e(t)y \right). \tag{14}$$

The signs result from the conventions defined in Fig. 1.

4.2 *Fatigue damage calculation*

The fatigue damage accumulation at the location of concern was calculated by rainflow counting the stress time series. The S-N curve was selected according to DNV recommendations [49] and defined by

$$\log(N) = \log(\bar{a}) - m \log\left(\Delta\sigma \left(\frac{t_c}{t_{ref}} \right)^k \right), \tag{15}$$

where N refers to the number of cycles to failure, $\Delta\sigma$ is the stress range, m is the negative inverse slope of the S-N curve, $\log(\bar{a})$ is the intercept of log N axis, t_{ref} is the reference thickness, t_c is the thickness through which a crack will most likely grow, k is the thickness exponent of fatigue strength. After using rainflow counting to bin the stress amplitudes into multiple stress levels and counting the number of cycles in every stress bin, respective damages for each stress bin were added using the Palmgren-Miner (PM) sum rule to obtain the total damage index D:

$$D = \sum_{i=1}^{N_c} \frac{n_i}{N_i}, \tag{16}$$

where n_i is the number of cycles in i^{th} stress bin, N_i is the number of cycles to fatigue failure for the nominal stress cycle amplitude i, and N_c is the total number of bins. To better quantify the fatigue damage, the fatigue damage index is normalized using a reference damage index D_{ref} which is the damage required in 10 minutes of simulation time that would lead to a total damage of 1 (failure according to PM sum rule) over 30 years. The normalized fatigue damage is denoted by $D_{norm} = D/D_{ref}$.

4.3 *Environmental states*

Table 3 Environmental states, based on data from ([51][21]).

State	V_w (m/s)	T_z (s)	H_s (m)	P_{State} (%)	State	V_w (m/s)	T_z (s)	H_s (m)	P_{State} (%)
1	4	3	0.5	3.95	12	14	5	2.0	3.26

2	4	4	0.5	3.21	13	16	4	2.0	1.79
3	6	3	0.5	11.17	14	16	5	2.5	3.10
4	6	4	0.5	7.22	15	18	5	2.5	1.74
5	8	3	0.5	11.45	16	18	5	3.0	0.80
6	8	4	1.0	8.68	17	20	5	2.5	0.43
7	10	3	0.5	5.31	18	20	5	3.0	1.14
8	10	4	1.0	11.33	19	22	5	3.0	0.40
9	12	4	1.0	5.86	20	22	6	4.0	0.29
10	12	4	1.5	6.00	21	24	5	3.5	0.15
11	14	4	1.5	4.48	22	24	6	4.0	0.10

A set of environmental states according to ([51][21]) was adopted to determine the load combinations and calculate the accumulated fatigue damage. Every combination of wind speed V_w, significant wave height H_s and zero-crossing wave period T_z corresponds to an occurrence probability P_{State}, as shown in Table 3. In line with the soil profile provided in Section 2.2, these environmental states are typical of a northern European offshore site. To obtain the JONSWAP spectrum, a relationship between the zero-crossing wave period and the peak wave period $T_p = 1.31T_z$ [52] was used. Wind speeds from 4 m/s to 24 m/s were grouped into 2 m/s bins. Wave heights and periods were grouped in 0.5 m and 1s bins, respectively. 22 environmental states were used to conduct the fatigue analysis. 91% of probability of occurrence is for the operational environmental states, with the remaining 9% corresponding to wind speeds below the cut-in speed and thus low contribution to fatigue damage. The wind and wave directionality in this study was simplified by assuming the wind and wave loads are in the same direction (see e.g. Koukoura et al. [3] for the influence of wind-wave misalignment). To represent the influence of the OWT control, the relationship between the mean wind speed, rotor rotation speed and blade pitch angles shown in Fig. 3 was adopted according to [36].

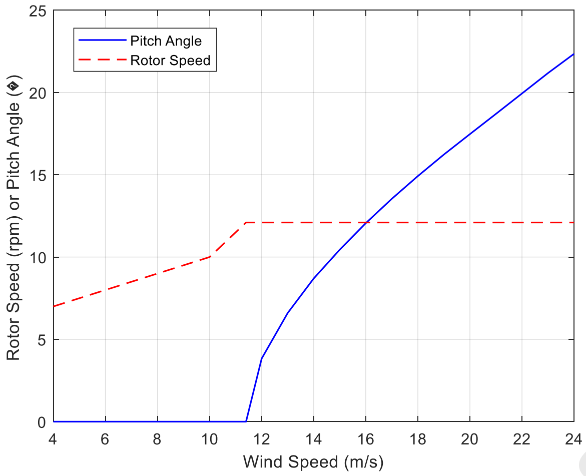

Fig. 3. Relationship between the rotor speed (dashed), pitch angle (solid) and inflow wind speed, based on [36].

5 Results and discussion

5.1 *Fatigue damage calculation for a single wind speed*

This section illustrates the fatigue calculation procedure for the 17th environmental state with a mean wind speed of 20 m/s and corresponding turbulence intensity according to the NTM. Simulations were performed for all environmental states (Table 3), with fatigue damage calculation results for the 9th environmental state (mean wind speed 12 m/s) shown in Appendix B.

The inflow wind field and wave profile were generated with the specified parameters and implemented as inputs to the fully coupled model. A 10-minute simulation with time step selected of 0.05s was first conducted with the fully coupled model. Then the fully coupled model was reduced to the 4-DOF model using the method described in Section 3. The dynamic responses of the support structure were obtained from the two models with the same time step. Fig. 4 compares the displacement responses at the tower top in the FA and SS directions obtained from the fully coupled model and the 4-DOF model. The difference between the responses from these two models can be explained by the fact that blade flexibility and structural damping are not considered in the 4-DOF model. However, the tower top responses generated by the fully coupled model and the 4-DOF model generally agree well in terms of dynamic amplitude and phase. The Time Response Assurance Criterion (TRAC) [53] is used here to quantify the degree of correlation between the two time histories. Considering two response vectors $\mathbf{u}_1(t)$ and $\mathbf{u}_2(t)$, the TRAC is defined as

$$TRAC = \frac{[\mathbf{u}_1(t)^{\mathrm{T}}\mathbf{u}_2(t)]^2}{[\mathbf{u}_1(t)^{\mathrm{T}}\mathbf{u}_1(t)][\mathbf{u}_2(t)^{\mathrm{T}}\mathbf{u}_2(t)]}, \quad (17)$$

where $\mathbf{u}_1(t)$ and $\mathbf{u}_2(t)$ have the same duration and time step. A TRAC value close to 1 indicates the two time histories are very similar. For the tower top displacement responses from the fully coupled model and the 4-DOF model in Fig. 4, the calculated TRAC values are 0.99 for the FA direction and 0.94 for the SS direction, indicating that the responses from these two models are very close.

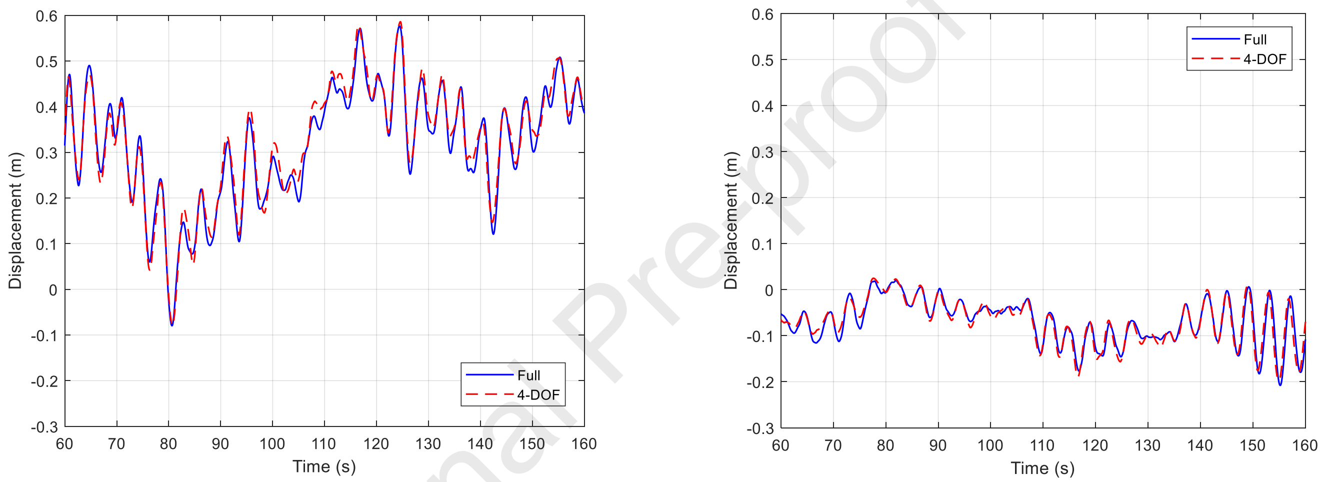

(a) (b)

Fig. 4. Comparison of the FA (a) and SS (b) displacement responses at the tower top between fully coupled model and the reduced 4-DOF model (17th environmental state, wind speed 20 m/s).

The Power Spectral Density (PSD) curves calculated from the FA tower top responses in Fig. 4(a) using the fully coupled model and the 4-DOF model are compared in Fig. 5(a). It can be seen that for the frequency range from 0 to 2 Hz these two curves agree very well. The FA response is dominated by the first bending mode of the support structure at approximately 0.25 Hz frequency. The influence of the 3P loading, which has a frequency of about 0.6 Hz, is observable in the frequency domain. The 17th environmental state corresponds to the rated rotor rotation speed of 12.1 rpm and a 0.2 Hz rotation frequency. Fig. 5(b) compares the PSD curves of the SS tower top responses in Fig. 4(b). For frequencies lower than 0.8 Hz, the two PSD curves agree well, confirming that the 4-DOF model successfully captures the OWT dynamic behaviour in the SS direction in this frequency range. The peak at the 3P frequency is clearer in this figure. However, the 4-DOF model does not capture the peak around 1.2 Hz which corresponds to the 6P loading [54] (the tracking of this peak at different wind speeds confirmed this). This is due to the aerodynamic decoupling which simplifies the wind-rotor interaction. Comparison between the two models was made for other environmental states in the frequency domain, from which it is evident that the 4-DOF model cannot capture frequency components related to higher multiples of the rotation frequency (6P, 12P, etc.) in the dynamic responses. Nevertheless, as the SS response is dominated by the first bending mode, not capturing the peak at 6P does not significantly influence the accuracy of the 4-DOF model in terms of dynamic response generation. This can be observed from the good agreement of the predicted vibration response in Fig. 4(b) and will be further demonstrated later for the fatigue damage prediction.

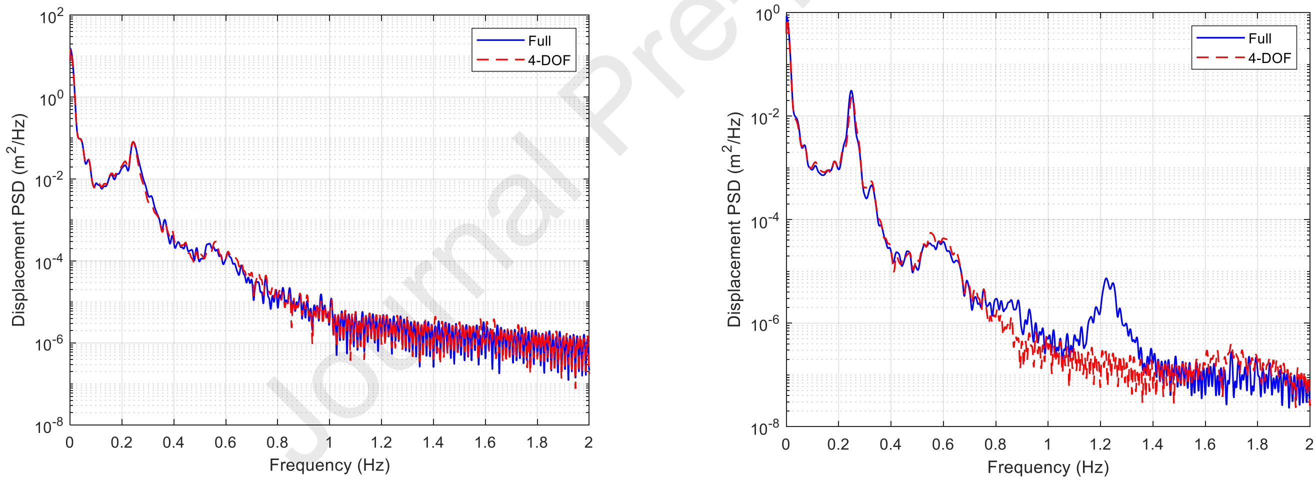

(a) (b)

Fig. 5. Comparison of the PSD curves of tower top displacement responses in the FA (a) and SS (b) directions obtained from the fully coupled model and the 4-DOF model (time series shown in Fig. 4).

For the fatigue calculation, it is necessary to obtain the stress time history at the hotspot. The location of the hotspot is selected at the position of the node at the mudline. Although the location where the moment reaches its maximum value can be below the mudline [21], the location at the mudline was picked for the purpose of illustrating the methodology. For the fully coupled model, the stress time history was obtained directly from the internal forces and beam section properties. For the 4-DOF model, the calculation of the stress time histories was based on modal expansion according to Eq. (14). At the selected section, the stress time history at the point where the fatigue damage index reaches its maximum is used to compare the two models, as shown in Fig. 6(a). Although there is some difference between the stress time histories, the fluctuations of the stresses are similar. The TRAC value for this stress time history comparison is 0.99, indicating that stresses calculated by these two models agree very well. In Fig. 6(b), the PSD curve of the maximum stress time history from the fully coupled model agrees well with that from the 4-DOF model in the frequency range from 0 to 1 Hz, showing that the 4-DOF model is able to capture similar dynamic behaviour in the dominant frequency range compared to the fully coupled model.

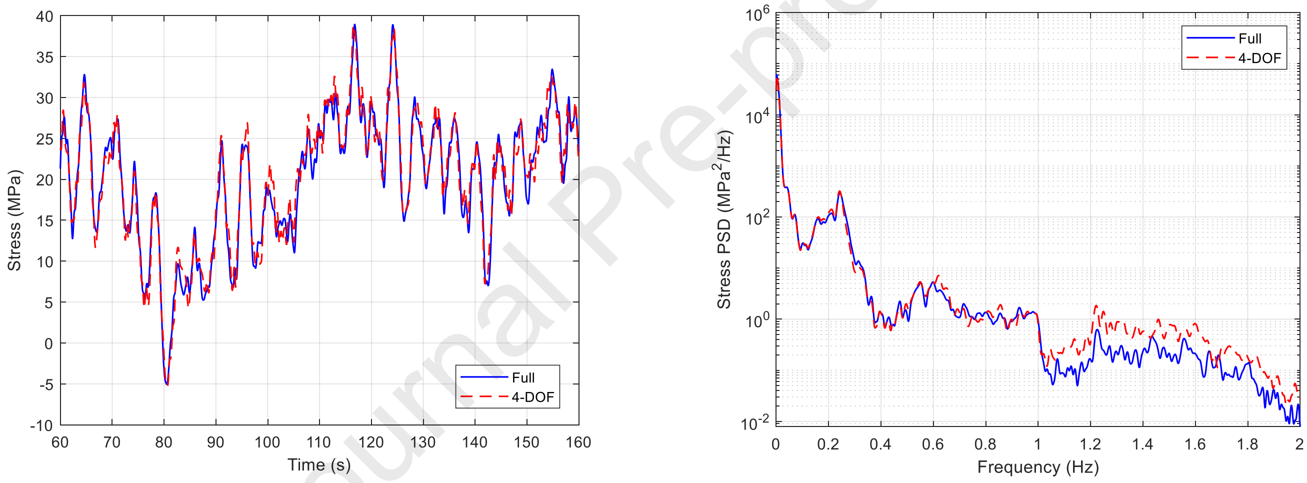

(a) (b)

Fig. 6. Comparison of the stress of the hotspot at the mudline from the fully coupled model and the 4-DOF model in the time domain (a) and frequency domain (b).

The normalised fatigue damage indexes corresponding to the stress time histories were obtained using the method described in Section 4.2. The normalised fatigue damage index and the computation duration are listed in Table 4. The calculated normalised damage indexes using the stress time histories from the two models are very close with a percentage difference of 3.7%. More importantly, the computation duration of the 4-DOF model is significantly shorter than that of the fully coupled model, demonstrating that the 4-DOF greatly outperforms the fully coupled model in terms of calculation speed. The computation speed of 4-DOF model is also significantly faster than that of OpenFAST [55], in spite of the latter modelling the blades and support structure by modal superposition, thereby reducing the number of DOFs.

Table 4 Normalised fatigue damage indexes and computation durations for the fully coupled model and the 4-DOF model (17^{th} environmental state, wind speed 20 m/s).

	Normalised damage	Computation duration (s)
Fully coupled model	5.47	2348
4-DOF model	5.27	13

5.2 *Fatigue life prediction*

This section compares fatigue life prediction results calculated by the fully coupled model and the 4-DOF model. The fatigue life prediction was based on the environmental states in Table 3. For each of the 22 environmental states, to reduce the influence of randomness in turbulent wind and irregular waves, the normalised fatigue damage index was calculated by averaging over simulations for 6 random seeds to generate the inflow wind fields and the wave profiles. 10-minute simulations were performed with the two models to obtain the stress time histories at the hotspot for each random seed. The selection of the number and length of simulations is according to IEC 61400-3 [45].

Fig. 7 compares the normalised damage indexes from the two models under different environmental states. For low wind speeds, the normalised damage indexes are much smaller than those with large wind speeds. Fig. 7 also shows the standard deviations of the normalised damage indexes from the responses for the 6 random seeds from the two models. It can be seen that for high environmental state numbers, the mean values and standard deviations for the two models are generally close. The influence of the random seed on the normalised fatigue damage index is relatively large for the higher environmental states, as the standard deviations are large. For the 22^{rd} environmental state for instance, the mean value of the normalised fatigue damage index is around 12.5 with a standard deviation of around 3 (24%). Fig. 8 compares the normalised damage contributions, which are the normalised damage indexes multiplied by the occurrence probabilities. Fatigue damage contributions are small for low wind speeds corresponding to environmental states 1 to 7. Overall, the fatigue damage calculation results by the two models are close.

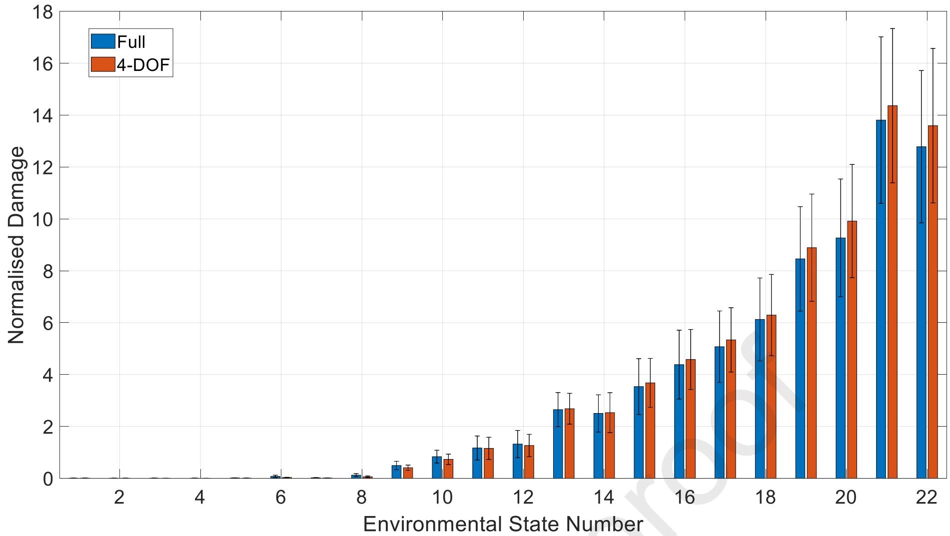

Fig. 7. Comparison of the normalised damage indexes from the fully coupled model and the 4-DOF model under different environmental states.

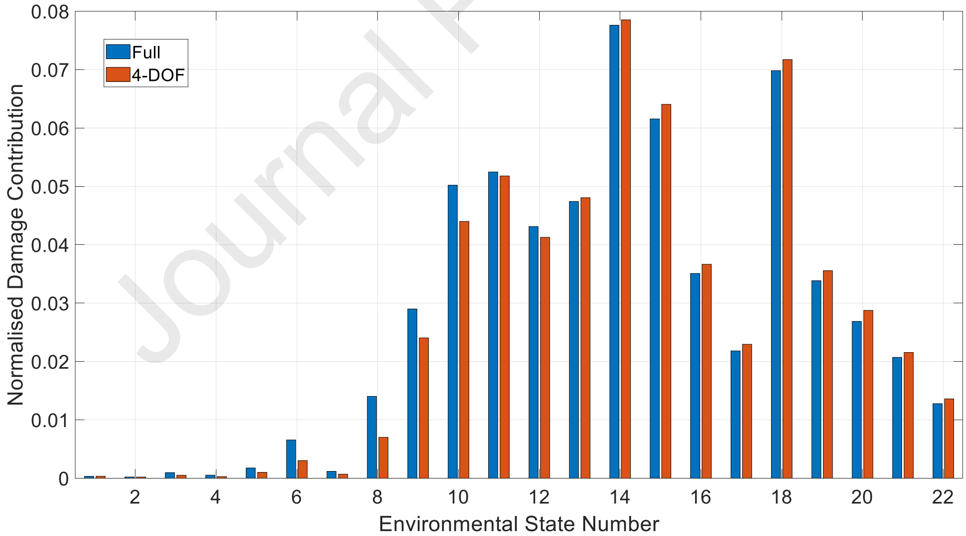

Fig. 8. Comparison of the normalised damage contributions from the fully coupled model and the 4-DOF model under different environmental states.

The percentage difference between the normalised damage indexes calculated by the two models can reach up to 40% for low environmental states (up to 8), corresponding to wind speeds lower than 12 m/s, probably due to the low absolute values of the damages. The percentage difference becomes much smaller (around 5%) for higher environmental states (from 11 to 22) corresponding to wind speeds larger than 12 m/s and these makes the most significant contribution to the fatigue life (as shown in Fig. 8).

Subsequently, the fatigue life was obtained according to Palmgren-Miner sum rule by combing the calculated fatigue damage indexes in 10 minutes and the occurrence probabilities of the environmental states. Table 5 lists the fatigue life predicted by the fully coupled model and the 4-DOF model for the assumed structural damping of 1.5%. These two models only result in 2% difference in terms of fatigue life prediction. The computation duration for the time integration of the fully coupled model is 84 hours, but the 4-DOF model only requires 30 minutes to complete the calculation.

Table 5 Fatigue damage indexes and computation durations for the fully coupled model and the 4-DOF model (1.5% structural and soil damping).

	Fatigue life (year)	Computation duration
Fully coupled model	49.4	84 hours
4-DOF model	50.4	30 min

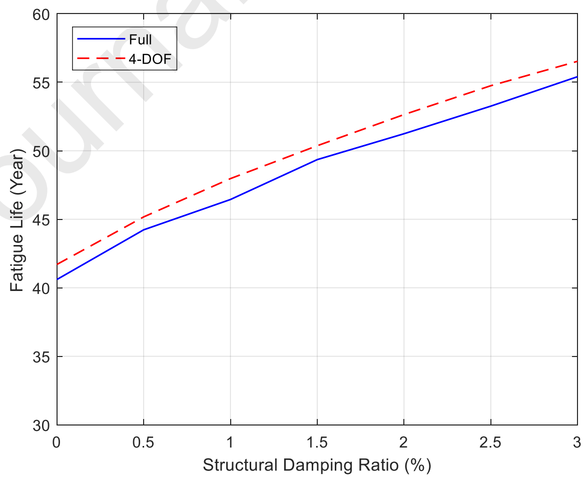

Fig. 9. Fatigue life prediction by the fully coupled model (blue, solid) and the 4-DOF model (red, dashed) for variation of the structural and soil damping.

A sensitivity analysis was conducted to study the influence of structural damping on the fatigue life prediction, to test how well this close match would hold for a wider range of input parameters. Damping ratios from 0 to 3% in 0.5% steps were assigned as the structural and soil damping of the OWT system, and the fatigue life was predicted using time series generated from the full and 4-DOF model for the same initial conditions (6 × 10-minute simulations). As shown in Fig. 9, the predicted fatigue life increases as the structural damping increases. The fatigue life predicted by the 4-DOF model follows the same trend very closely and is consistently approximately 1-year larger than that from the fully coupled model, with a maximum difference of 1.5 years. Given the uncertainty around standard fatigue life calculations, this consistently small difference is not significant and indicates that the reduced model can be used to carry out fatigue life assessments at a much-reduced computational cost.

5.3 *Discussion of modelling assumptions*

Combining the aerodynamic decoupling and modal reduction introduced in Sections 3.1 and 3.2 simplifies the fully coupled model into a numerically efficient modal model. This process is underpinned by some assumptions, including rigid blades, lumped RNA mass at the tower top, and limited modes dominating the low-frequency vibration response in OWTs. More details of these assumptions can be found in references [35] and [48]. Among these assumptions, the rigid blade assumption is potentially the most problematic. However, it was demonstrated in [35] that assuming rigid blades does not significantly alter the aerodynamic damping contribution and only has a limited impact on the overall natural frequencies of the wind turbine system. The effect of the number of modes required to carry out the fatigue analysis was investigated as discussed in Section 3.2 and it was found that the 4-DOF mode, considering the first two bending modes, provides the best compromise between computational speed and accuracy.

The methodology was developed around a specific case study that can easily be extended or adapted to analyse other wind turbine systems such as fixed-bottom, three-bladed, horizontal axis OWTs of various sizes supported with different foundation types and considering wind, wave and tidal conditions.

6 **Conclusions**

This study proposes a computationally efficient fatigue life prediction methodology for offshore wind turbines based on a recently developed aerodynamic decoupling strategy and modal reduction. A fully coupled model can be reduced to a 4-DOF model, thereby significantly decreasing the number of DOFs in the OWT system, while considering all relevant features such as soil-structure interaction and key dynamic couplings. Combining modal expansion and a method to extract the stresses from nodal displacements, the stress time histories at the hotspot can be calculated efficiently using the 4-DOF model. The fatigue life of a reference 5 MW model OWT was predicted considering typical northern European environmental states, using both a fully coupled model and the reduced model. Results show that the 4-DOF model accurately predicts fatigue damage and provides very close fatigue life prediction results compared to the fully coupled model. A structural damping sensitivity study was carried out and confirms that fatigue life predictions consistently matched within 2% for a range of parameters. The good accuracy of the reduced model can be attributed to the ability of the unconventional aerodynamic damping matrix, upon which it is based, to better capture the coupling between the FA and SS directions than conventional damping ratios.

In addition to accuracy, a significant advantage of the proposed fatigue life methodology is its numerical efficiency and rapid computational speed. Compared to the fully coupled model, aerodynamic decoupling and modal expansion significantly reduce the required DOFs to be considered in the time integration. As a result, the duration of the time integration for the modal model is around 0.5% of that for the fully coupled model. Therefore, the proposed fatigue life prediction methodology has the potential to be applied in the preliminary design practice to quickly estimate the fatigue life of OWTs. In practical fatigue life assessment of OWTs, the proposed methodology could be advantageous, as reducing the analysis time is demanding with many environmental states and load combinations to be considered. Employing the proposed methodology, a more comprehensive fatigue life prediction with increased numbers of load cases and parameter variation studies can be conducted. The proposed model could be used to predict the influence of variations, e.g., of scour, mean sea level, tidal conditions, or changes to the turbine size and support structure. Some design procedures require a large number of dynamic response calculations, such as Monte Carlo-based fatigue reliability analysis or structural/control optimisation. Further research should consider the comparison and validation against experimental data for deployed offshore wind turbines and the extension to consider the flexibility and fatigue life prediction of wind turbine blades.

7 Acknowledgement

Financial support from the National Science Fund for Distinguished Young Scholars (No. 52025082) and the National Natural Science Foundation of China (No. 51908209) are greatly appreciated. The financial support to the first author from Dr. Feipeng Liu of Northwest Engineering Corporation Limited through a research project (No. H202194370223) is also acknowledged.

References

[1] Oest J, Rene Sørensen, Lars LC, et al. Structural optimization with fatigue and ultimate limit constraints of jacket structures for large offshore wind turbines. *Struct Multidiscip Optim* 2017; 55: 779–793.

[2] Yuan Y, Tang J. On Advanced Control Methods toward Power Capture and Load Mitigation in Wind Turbines. *Engineering* 2017; 3: 494–503.

[3] Koukoura C, Brown C, Natarajan A, et al. Cross-wind fatigue analysis of a full scale offshore wind turbine in the case of wind–wave misalignment. *Eng Struct* 2016; 120: 147–157.

[4] Torben J, Melchior A. *How 2 HAWC2, the user's manual*. Technical Report Risø-R-1597(ver. 3-1)(EN). Risø National Laboratory, Denmark, 2007.

[5] Velarde J, Kramhøft C, Sørensen JD. Global sensitivity analysis of offshore wind turbine foundation fatigue loads. *Renew Energy* 2019; 140: 177–189.

[6] Velarde J, Kramhøft C, Sørensen JD, et al. Fatigue reliability of large monopiles for offshore wind turbines. *Int J Fatigue* 2020; 134: 105487.

[7] Marino E, Giusti A, Manuel L. Offshore wind turbine fatigue loads: The influence of alternative wave modeling for different turbulent and mean winds. *Renew Energy* 2017; 102: 157–169.

[8] Jonkman JM, Buhl MLJ. *FAST user's guide*. Technical Report NREL/EL-500-38230. National Renewable Energy Laboratory: Golden, CO, USA, October 2005.

[9] Hübler C, Gebhardt CG, Rolfes R. Methodologies for fatigue assessment of offshore wind turbines considering scattering environmental conditions and the uncertainty due to finite sampling. *Wind Energy* 2018; 21: 1092–1105.

[10] Horn JT, Leira BJ. Fatigue reliability assessment of offshore wind turbines with stochastic availability. *Reliab Eng Syst Saf* 2019; 191: 106550.

[11] Stieng LES, Muskulus M. Reducing the number of load cases for fatigue damage assessment of offshore wind turbine support structures using a simple severity-based sampling method. *Wind Energy Sci* 2018; 3: 805–818.

[12] Huchet Q, Mattrand C, Beaurepaire P, et al. AK-DA: An efficient method for the fatigue assessment of wind turbine structures. *Wind Energy* 2019; 22: 638–652.

[13] Zwick D, Muskulus M. Simplified fatigue load assessment in offshore wind turbine structural analysis. *Wind Energy* 2016; 19: 265–278.

[14] Häfele J, Hübler C, Gebhardt CG, et al. A comprehensive fatigue load set reduction study for offshore wind turbines with jacket substructures. *Renew Energy* 2018; 118: 99–112.

[15] Stieng LES, Muskulus M. Load case reduction for offshore wind turbine support structure fatigue assessment by importance sampling with two-stage filtering. *Wind Energy* 2019; 22: 1472–1486.

[16] Wilkie D, Galasso C. Gaussian process regression for fatigue reliability analysis of offshore wind turbines. *Struct Saf* 2021; 88: 102020.

[17] Yeter B, Garbatov Y, Guedes Soares C. Evaluation of fatigue damage model predictions for fixed offshore wind turbine support structures. *Int J Fatigue* 2016; 87: 71–80.

[18] Bisoi S, Haldar S. Dynamic analysis of offshore wind turbine in clay considering soil–monopile–tower interaction. *Soil Dyn Earthq Eng* 2014; 63: 19–35.

[19] Dong W, Moan T, Gao Z. Fatigue reliability analysis of the jacket support structure for offshore wind turbine considering the effect of corrosion and inspection. *Reliab Eng Syst Saf* 2012; 106: 11–27.

[20] Dong W, Moan T, Gao Z. Long-term fatigue analysis of multi-planar tubular joints for jacket-type offshore wind turbine in time domain. *Eng Struct* 2011; 33: 2002–2014.

[21] Rezaei R, Fromme P, Duffour P. Fatigue life sensitivity of monopile-supported offshore wind turbines to damping. *Renew Energy* 2018; 123: 450–459.

[22] Rezaei R, Duffour P, Fromme P. Scour influence on the fatigue life of operational monopile-supported offshore wind turbines. *Wind Energy* 2018; 1–14.

[23] Muskulus M. Simplified rotor load models and fatigue damage estimates for offshore wind turbines. *Philos Trans R Soc London A Math Phys Eng Sci* 2015; 373: 20140347.

[24] Schafhirt S, Muskulus M. Decoupled simulations of offshore wind turbines with reduced rotor loads and aerodynamic damping. *Wind Energy Sci* 2018; 3: 25.

[25] Salzmann DJC, Tempel J Van Der. Aerodynamic damping in the design of support structures for offshore wind turbines. In: *The European Offshore Wind Conference & Exhibition*. Copenhagen, Denmark, 2005.

[26] Valamanesh V, Myers AT. Aerodynamic damping and seismic response of horizontal axis wind turbine towers. *J Struct Eng* 2014; 140: 1–9.

[27] Liu X, Lu C, Li G, et al. Effects of aerodynamic damping on the tower load of offshore horizontal axis wind turbines. *Appl Energy* 2017; 204: 1101–1114.

[28] Hansen MH, Thomsen K, Fuglsang P, et al. Two methods for estimating aeroelastic damping of operational wind turbine modes from experiments. *Wind Energy* 2006; 9: 179–191.

[29] Ozbek M, Rixen DJ. Operational modal analysis of a 2.5 MW wind turbine using optical measurement techniques and strain gauges. *Wind Energy* 2013; 17: 367–381.

[30] Koukoura C, Natarajan A, Vesth A. Identification of support structure damping of a full scale offshore wind turbine in normal operation. *Renew Energy* 2015; 81: 882–895.

[31] Dai K, Wang Y, Huang Y, et al. Development of a modified stochastic subspace identification method for rapid structural assessment of in-service utility-scale wind turbine towers. *Wind Energy* 2017; 17: 657–669.

[32] Dong X, Lian J, Wang H, et al. Structural vibration monitoring and operational modal analysis of offshore wind turbine structure. *Ocean Eng* 2018; 150: 280–297.

[33] Tarp-Johansen NJ, Andersen L, Christensen ED, et al. Comparing sources of damping of cross-wind motion. In: *Proceeding of the Copenhagen Offshore Conference*. Stockholm, Sweden, 2009.

[34] Chen C, Duffour P, Fromme P. Novel aerodynamic damping identification method for operating wind turbines. *J Phys Conf Ser* 2019; 1222: 012008.

[35] Chen C, Duffour P, Fromme P. Modelling wind turbine tower-rotor interaction through an aerodynamic damping matrix. *J Sound Vib* 2020; 489: 115667.

[36] Jonkman JM, Butterfield S, Musial W, et al. *Definition of a 5-MW reference wind turbine for offshore system development*. Technical Report NREL/TP-500-38060. National Renewable Energy Laboratory: Golden, CO, USA, 2009.

[37] Staino A, Basu B. Dynamics and control of vibrations in wind turbines with variable rotor speed. *Eng Struct* 2013; 56: 58–67.

[38] Chen C, Duffour P. Modelling damping sources in monopile-supported offshore wind turbines. *Wind Energy* 2018; 21: 1121–1140.

[39] Gavin HP. *Numerical integration in structural dynamics*. Duke University,

http://people.duke.edu/~hpgavin/cee541/NumericalIntegration.pdf (2016).

[40] Subramanian N. *Steel structures - design and practice*. Oxford University Press, 2011.

[41] DNV GL. *DNVGL-RP-C212 Offshore soil mechanics and geotechnical engineering*. 2017.

[42] Hansen M. *Aerodynamics of wind turbines*. Second Edi. Routledge, 2008.

[43] Branlard E. Chapter 10 The Blade ElementMomentum (BEM) Method. In: *Wind Turbine Aerodynamics and Vorticity-Based Methods*. Epub ahead of print 2017. DOI: 10.1007/978-3-319-55164-7.

[44] Jonkman BJ, Kilcher L. *TurbSim user's guide : version 1. 06.00*. Technical Report. National Renewable Energy Laboratory: Golden, CO, USA, 2012.

[45] International Electrotechnical Commission (IEC). *IEC 61400-3 Wind turbines - Part 3: Design requirements for offshore wind turbines*. 2009.

[46] Shirzadeh R, Devriendt C, Bidakhvidi MA, et al. Experimental and computational damping estimation of an offshore wind turbine on a monopile foundation. *J Wind Eng Ind Aerodyn* 2013; 120: 96–106.

[47] Hasselmann K, Barnett TP, Bouws E, et al. Measurements of wind-wave growth and swell decay during the Joint North Sea Wave Project (JONSWAP). *Ergnzungsh zur Dtsch Hydrogr Zeitschrift R* 1973; A(8): 1–95.

[48] Chen C, Duffour P, Dai K, et al. Identification of aerodynamic damping matrix for operating wind turbines. *Mech Syst Signal Process* 2021; 154: 107568.

[49] DNV. RP-C203- Fatigue design of offshore steel structures. *Recomm Pract DNV-RPC203* 2014; 126.

[50] Pelayo F, Skafte A, Aenlle ML, et al. Modal Analysis Based Stress Estimation for Structural Elements Subjected to Operational Dynamic Loadings. *Exp Mech* 2015; 55: 1791–1802.

[51] Tempel J Van Der. *Design of support structures for offshore wind turbines*. PhD Thesis. Delft University of Technology, 2006.

[52] Baniotopoulos C, Borri C, Stathopoulos T. *Environmental wind engineering and design of wind energy structures*. Springer Science & Business Media, 2011.

[53] Avitabile P, Pingle P. Prediction of full field dynamic strain from limited sets of measured data. *Shock Vib* 2012; 19: 765–785.

[54] Sønderby I, Hansen MH. Open-loop frequency response analysis of a wind

turbine using a high-order linear aeroelastic model. *Wind Energy* 2014; 17: 1147–1167.

[55] National Renewable Energy Laboratory (NREL). OpenFAST Documentation - Release v2.3.0, https://readthedocs.org/projects/openfast/downloads/pdf/master/ (2020).

Appendix A

To consider a non-uniform inflow wind field, some modifications are needed to the derivation process described in Section 3.3 of reference [35]. Keeping the initial assumptions that the rotor is rigid and the RNA speed is small, the aerodynamic forces applied to one blade element can be expressed by Eqs. (4) to (7) in [35]. However, when summing up the elemental blade forces for one blade, the three blades must be considered individually, as the total aerodynamic forces experienced by different blades are different due to wind turbulence and different azimuthal positions. In this way, the aerodynamic force resultants can still be linearised as forces applied to a rigid tower plus terms related to the tower top velocities. Using the notations introduced in [35], the total force at the tower top in the x (FA) direction can be expressed as the sum of thrusts applied to all blades:

$$\begin{aligned} F_x^{Flex}(t) &= \sum_{i=1}^{N_b} \int_0^R dT(V_{xRel}, V_{rRel}) \\ &= \sum_{i=1}^{N_b} \int_0^R dT(V_0, V_r) - \dot{x} \sum_{i=1}^{N_b} \int_0^R \frac{\partial(dT)}{\partial V_0} - \dot{\theta}_y \sum_{i=1}^{N_b} cos\gamma_i(t) \int_0^R r \frac{\partial(dT)}{\partial V_0} \\ &- \dot{y} \sum_{i=1}^{N_b} cos\gamma_i(t) \int_0^R \frac{\partial(dT)}{\partial V_r} + \dot{\theta}_x \sum_{i=1}^{N_b} \int_0^R r \frac{\partial(dT)}{\partial V_r}. \end{aligned} \tag{A. 1}$$

The total force in the y (SS) direction is:

$$\begin{aligned} F_y^{Flex}(t) &= -\sum_{i=1}^{N_b} cos\gamma_i(t) \int_0^R dS(V_{xRel}, V_{rRel}) \\ &= -\sum_{i=1}^{N_b} cos\gamma_i(t) \int_0^R dS(V_0, V_r) + \dot{x} \sum_{i=1}^{N_b} \cos\gamma_i(t) \int_0^R \frac{\partial(dS)}{\partial V_0} \\ &+ \dot{\theta}_y \sum_{i=1}^{N_b} \cos^2\gamma_i(t) \int_0^R r \frac{\partial(dS)}{\partial V_0} + \dot{y} \sum_{i=1}^{N_b} \cos^2\gamma_i(t) \int_0^R \frac{\partial(dS)}{\partial V_r} \\ &- \dot{\theta}_x \sum_{i=1}^{N_b} cos\gamma_i(t) \int_0^R r \frac{\partial(dS)}{\partial V_r}. \end{aligned} \tag{A. 2}$$

The total moment about the x axis is:

$$M_x^{Flex}(t) = \sum_{i=1}^{N_b} \int_0^R dM_x(V_{xRel}, V_{rRel}) \tag{A. 3}$$

$$= \sum_{i=1}^{N_b} \int_0^R r dS(V_0, V_r) - \dot{x} \sum_{i=1}^{N_b} \int_0^R r \frac{\partial(dS)}{\partial V_0}$$
$$- \dot{\theta}_y \sum_{i=1}^{N_b} cos\gamma_i(t) \int_0^R r^2 \frac{\partial(dS)}{\partial V_0}$$
$$-\dot{y} \sum_{i=1}^{N_b} cos\gamma_i(t) \int_0^R r \frac{\partial(dS)}{\partial V_r} + \dot{\theta}_x \sum_{i=1}^{N_b} \int_0^R r^2 \frac{\partial(dS)}{\partial V_r},$$

whereas the total moment about the y axis is:

$$M_y^{Flex}(t) = \sum_{i=1}^{N_b} \int_0^R dM_y(V_{xRel}, V_{rRel})$$
$$= \sum_{i=1}^{N_b} cos\gamma_i(t) \int_0^R r dT(V_0, V_r) - \dot{x} \sum_{i=1}^{N_b} cos\gamma_i(t) \int_0^R r \frac{\partial(dT)}{\partial V_0} \quad \text{(A. 4)}$$
$$-\dot{\theta}_y \sum_{i=1}^{N_b} \cos^2\gamma_i(t) \int_0^R r^2 \frac{\partial(dT)}{\partial V_0} - \dot{y} \sum_{i=1}^{N_b} \cos^2\gamma_i(t) \int_0^R r \frac{\partial(dT)}{\partial V_r}$$
$$+\dot{\theta}_x \sum_{i=1}^{N_b} cos\gamma_i(t) \int_0^R r^2 \frac{\partial(dT)}{\partial V_r}.$$

The derivatives in Equations (A. 1) to (A. 4) can be found using expressions of partial derivatives in Appendix A in [35]. According to Equations (A. 1) to (A. 4), the resultant aerodynamic forces from the rotor to the top of a flexible wind turbine tower, $\mathbf{F}_{Flex}^{Top}(t) = \left[F_x^{Flex}(t)\ F_y^{Flex}(t)\ M_x^{Flex}(t)\ M_y^{Flex}(t)\right]^T$, can be rewritten in the following simplified form

$$\mathbf{F}_{Flex}^{Top}(t) = \begin{bmatrix} \sum_{i=1}^{N_b} \int_0^R dT(V_0, V_r) \\ -\sum_{i=1}^{N_b} cos\gamma_i(t) \int_0^R dS(V_0, V_r) \\ \sum_{i=1}^{N_b} \int_0^R r dS(V_0, V_r) \\ \sum_{i=1}^{N_b} cos\gamma_i(t) \int_0^R r dT(V_0, V_r) \end{bmatrix} - \mathbf{C}_{Aero} \begin{bmatrix} \dot{x} \\ \dot{y} \\ \dot{\theta}_x \\ \dot{\theta}_y \end{bmatrix} = \mathbf{F}_{Rigid}^{Top}(t) - \mathbf{C}_{Aero}\dot{\mathbf{u}}^{Top}(t), \quad \text{(A. 5)}$$

where

$$\mathbf{C}_{Aero} =$$

$$\begin{bmatrix} \sum_{i=1}^{N_b}\int_0^R \frac{\partial(dT)}{\partial V_0} & \sum_{i=1}^{N_b} cos\gamma_i(t)\int_0^R \frac{\partial(dT)}{\partial V_r} & -\sum_{i=1}^{N_b}\int_0^R r\frac{\partial(dT)}{\partial V_r} & \sum_{i=1}^{N_b} cos\gamma_i(t)\int_0^R r\frac{\partial(dT)}{\partial V_0} \\ -\sum_{i=1}^{N_b}\cos\gamma_i(t)\int_0^R \frac{\partial(dS)}{\partial V_0} & -\sum_{i=1}^{N_b}\cos^2\gamma_i(t)\int_0^R \frac{\partial(dS)}{\partial V_r} & \sum_{i=1}^{N_b} cos\gamma_i(t)\int_0^R r\frac{\partial(dS)}{\partial V_r} & -\sum_{i=1}^{N_b}\cos^2\gamma_i(t)\int_0^R r\frac{\partial(dS)}{\partial V_0} \\ \sum_{i=1}^{N_b}\int_0^R r\frac{\partial(dS)}{\partial V_0} & \sum_{i=1}^{N_b} cos\gamma_i(t)\int_0^R r\frac{\partial(dS)}{\partial V_r} & -\sum_{i=1}^{N_b}\int_0^R r^2\frac{\partial(dS)}{\partial V_r} & \sum_{i=1}^{N_b} cos\gamma_i(t)\int_0^R r^2\frac{\partial(dS)}{\partial V_0} \\ \sum_{i=1}^{N_b} cos\gamma_i(t)\int_0^R r\frac{\partial(dT)}{\partial V_0} & \sum_{i=1}^{N_b}\cos^2\gamma_i(t)\int_0^R r\frac{\partial(dT)}{\partial V_r} & -\sum_{i=1}^{N_b} cos\gamma_i(t)\int_0^R r^2\frac{\partial(dT)}{\partial V_r} & \sum_{i=1}^{N_b}\cos^2\gamma_i(t)\int_0^R r^2\frac{\partial(dT)}{\partial V_0} \end{bmatrix}. \quad (A.\ 6)$$

$\mathbf{C}_{Aero}$ can be written more concisely:

$$\mathbf{C}_{Aero} = \begin{bmatrix} c_{xx} & c_{xy} & c_{x\theta_x} & c_{x\theta_y} \\ c_{yx} & c_{yy} & c_{y\theta_x} & c_{y\theta_y} \\ c_{\theta_x x} & c_{\theta_x y} & c_{\theta_x\theta_x} & c_{\theta_x\theta_y} \\ c_{\theta_y x} & c_{\theta_y y} & c_{\theta_y\theta_x} & c_{\theta_y\theta_y} \end{bmatrix}. \quad (A.\ 7)$$

Appendix B

Simulations were conducted for all environmental states (Table 3), with Section 5.1 showing the fatigue calculation procedure for the 17th environmental state with a relatively high mean wind speed of 20 m/s. The fatigue damage calculation results are demonstrated here for the 9th environmental state, corresponding to a mean wind speed of 12 m/s, near the rated wind speed (11.4 m/s) of the considered OWT.

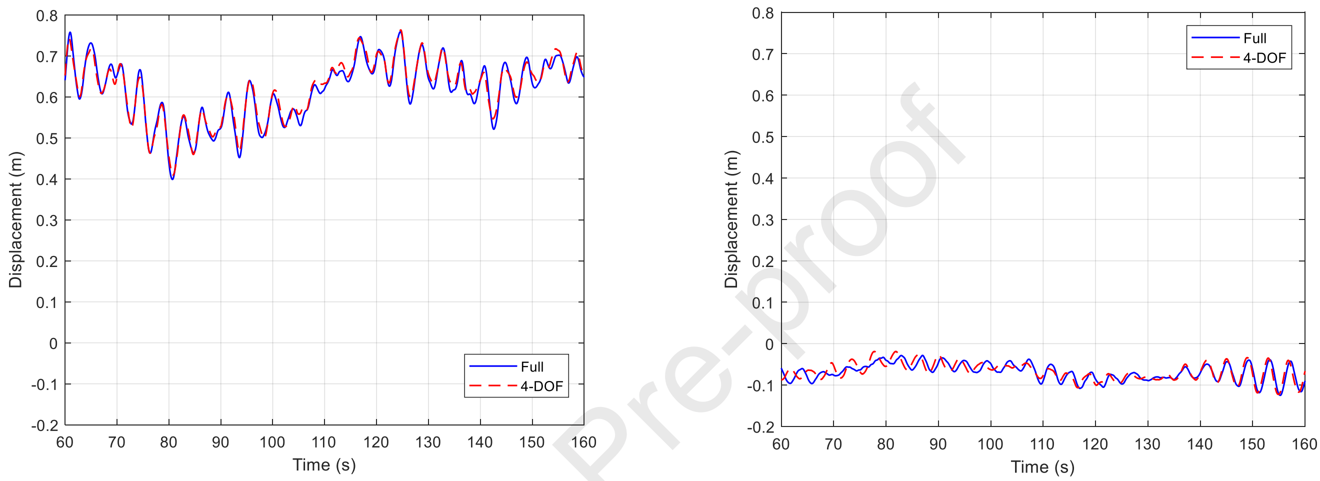

(a) (b)

Fig. B1. Comparison of the FA (a) and SS (b) displacement responses at the tower top between fully coupled model and the reduced 4-DOF model (9th environmental state, wind speed 12 m/s).

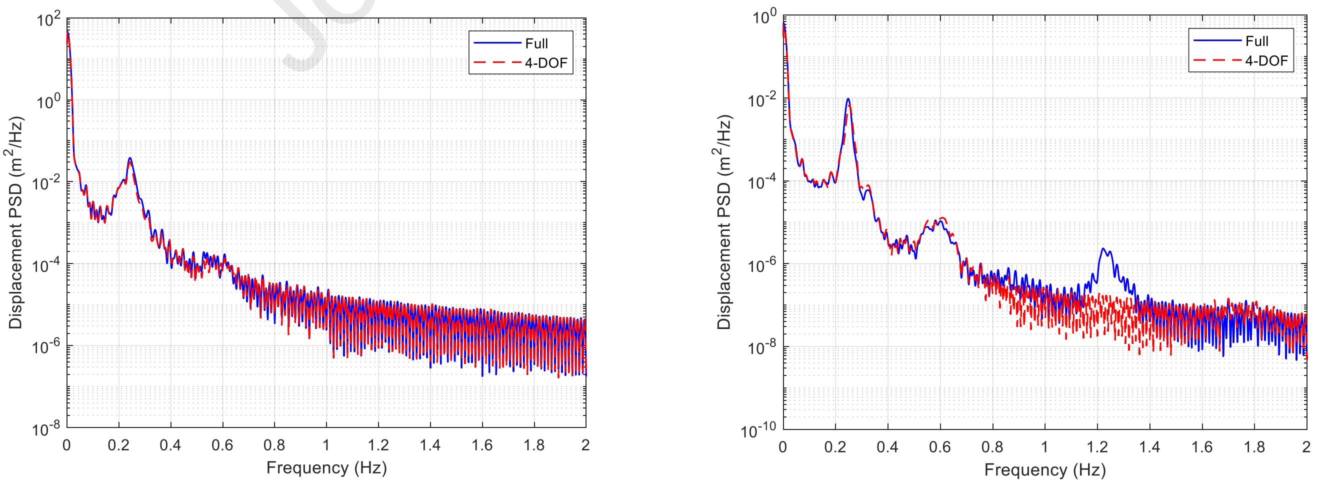

(a) (b)

Fig. B2. Comparison of the PSD curves of tower top displacement responses in the FA (a) and SS (b) directions obtained from the fully coupled model and the 4-DOF model (time series shown in Fig. B1).

Fig. B1 compares the tower top displacement responses in the FA and SS directions obtained from the fully coupled model and the 4-DOF model, with good agreement and TRAC values of 0.99 for the FA direction and 0.96 for the SS direction. These are comparable to the respective TRAC values of 0.99 (FA direction) and 0.94 (SS direction) obtained in Section 5.1 for a wind speed of 20 m/s (17th environmental state). Fig. B2 shows the comparison of the tower top responses in the frequency domain. It shows that the responses generated by the two models are overall very similar in both the time and frequency domain. However, as observed in Section 5.1 (Fig. 5(b)), the 4-DOF model cannot capture the 6P peak at 1.2 Hz. The maximum stress time histories at the hotspot obtained from the fully coupled model and the 4-DOF model are compared in Fig. B3(a), with a TRAC value of 0.99. In Fig. B3(b) the maximum stress time histories obtained from these two models are compared in the frequency domain, showing that the two models predict very similar stresses at the hotspot, especially up to a frequency of 1 Hz (similar to Fig. 6). The normalised fatigue damage index and the computation duration are listed in Table B1, demonstrating that the 4-DOF model is able to predict fatigue damage accurately and very quickly compared to the fully coupled model.

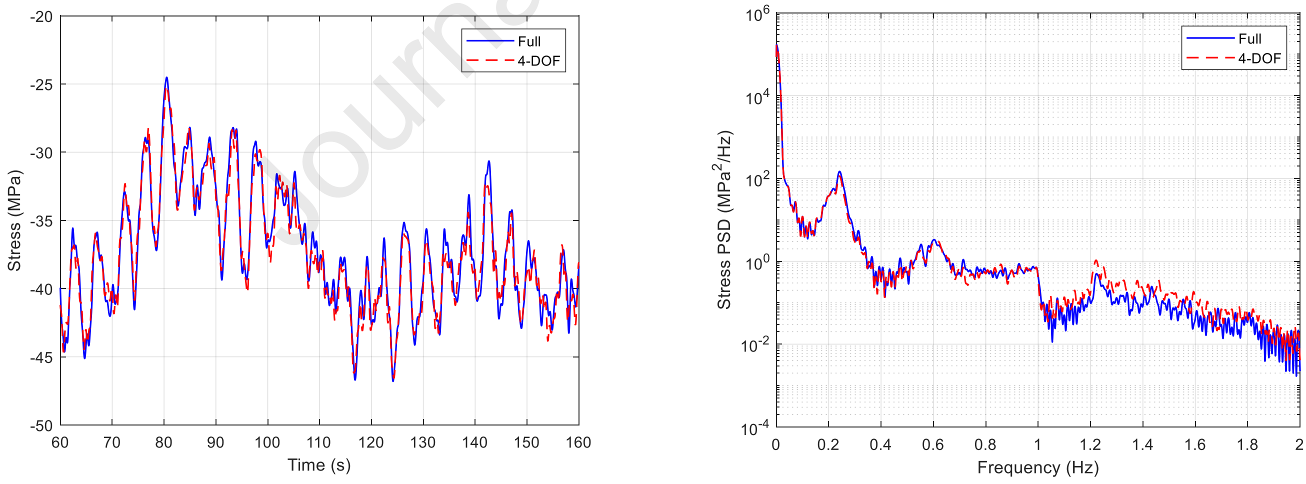

(a) (b)

Fig. B3. Comparison of the stress of the hotspot at the mudline from the fully coupled model and the 4-DOF model in the time domain (a) and frequency domain (b).

Table B1 Normalised fatigue damage indexes and computation duration for the fully coupled model and the 4-DOF model (9th environmental state, wind speed 12 m/s).

	Normalised damage	Computation duration (s)
Fully coupled model	5.60	2350
4-DOF model	5.11	13

Declaration of interests

☒ The authors declare that they have no known competing financial interests or personal relationships that could have appeared to influence the work reported in this paper.

☐The authors declare the following financial interests/personal relationships which may be considered as potential competing interests: